This article has been accepted for publication in a future issue of this journal, but has not been fully edited. Content may change prior to final publication. Citation information: DOI 10.1109/TPEL.2021.3089282, IEEE Transactions on Power Electronics

Robust Active Damping Strategy for DFIG Wind Turbines

Leyre Rosado, *Student Member, IEEE,* Javier Samanes, *Member, IEEE,* Eugenio Gubía, *Member, IEEE,* and Jesús López, *Member, IEEE,*

***Abstract*—Doubly-fed induction generators (DFIG) with *LCL* filter are widely used for wind power generation. In these energy conversion systems, there is an interaction between the grid side converter (GSC) and the rotor side converter (RSC) control loops, the generator and the *LCL* filter that must be properly modeled. Such interaction between the GSC and the RSC proves to have a significant influence on the stability. Several active damping (AD) methods for grid-connected converters with *LCL* filter have been proposed, nevertheless, the application of these techniques to a DFIG wind turbine is not straightforward, as revealed in this work. To achieve a robust damping irrespective of the grid inductance, this paper proposes an AD strategy based on the capacitor current feedback and the adjustment of the control delays to emulate a virtual impedance, in parallel with the filter capacitor, with a dominant resistive component in the range of possible resonance frequencies. This work also proves that, by applying the AD strategy in both converters simultaneously, the damping of the system resonant poles is maximized when a specific value of the grid inductance is considered. Experimental results show the interaction between the GSC and the RSC and validate the proposed AD strategy.**

***Index Terms*—Active damping, Doubly-fed induction generator, *LCL* filter, Stability analysis, Virtual impedance.**

I. Introduction

DOUBLY-fed induction generators with *LCL* filter are widely used in commercial wind energy conversion systems (WECS) [1], [2]. In this configuration, the stator windings are directly connected to the grid, whereas a back-to-back power converter is employed in the rotor circuit. Its rated power is around 30% of the rated generator power, leading to lower cost and lower power losses compared to full converter wind turbines using synchronous generators. The overall system cost can be further reduced if an *LCL* filter is used to comply with the grid codes and attenuate the high-frequency harmonics, compared to an *L* filter [3].

However, the resonance of the *LCL* filter and its interaction with the converter control may cause stability problems, which can be solved by means of passive [4] or active damping techniques [5]. Passive damping methods use additional damping resistors connected in series or in parallel with the filter components, increasing power losses. Active damping methods are a preferred option, as they modify the control loop in order to guarantee system stability at no additional cost or power loss.

Active damping methods have been widely discussed in the literature for grid-connected converters with *LCL* filter so they serve as background for this work. One common AD method is the capacitor voltage feedforward. It highly simplifies the plant to be controlled, which becomes equal to the converter inductor admittance [6]. However, due to the delays of the digital control loop, it may destabilize the system as the *LCL* resonance frequency becomes closer to the controller sampling frequency [7].

Another method consists of introducing filters in cascade with the current controller, such as notch filters, lead-lag compensators or low pass filters [8]–[10]. It is a simple technique since it does not require additional sensors. However, the control bandwidth can be reduced when the resonance frequency becomes closer to the controller bandwidth. It may also be less effective in case of resonance frequency drifts caused by changes in the value of the grid inductance or changes in the *LCL* filter parameters due to ageing or parameter tolerances. Besides, it does not provide sufficient damping to the resonant poles to comply with current harmonic limits imposed by grid codes [11].

All-pass filters in series with the current controller can also be used to reshape the open-loop phase so that the closed-loop system is stable. The open-loop phase can be made equal to zero at the resonance frequency using a first order all-pass filter [12] but it slows down the transient response. As an alternative, a second order filter could be used but, in this case, the system is less robust when it is connected to a weak grid. In [13] a stable region is identified for a given range of grid impedance and *LCL* filter parameter variations, when the grid current is controlled. Then, the all-pass filter is used to move the open-loop phase into this region. However, as specified by the authors, this method is not very suitable for the inverter current control because, for typical *LCL* filter parameters, a phase lead is required and the instability may be shifted to higher frequencies.

A different approach is based on the capacitor current proportional feedback, which is equivalent to a virtual resistor in parallel with the filter capacitor [14]. However, due to the delay of the digital control loop and the measurement filters, the virtual resistor becomes a virtual impedance [15]. If the resonance frequency is located in the range where the virtual

L. Rosado is with the Department of Electrical and Electronic Engineering and the Institute of Smart Cities, Public University of Navarre, 31006, Navarre, Spain (e-mail: leyre.rosado@unavarra.es), corresponding author.

J. Samanes is with the Department of Electrical and Electronic Engineering and the Institute of Smart Cities, Public University of Navarre, 31006, Navarre, Spain (e-mail: javier.samanes@unavarra.es).

E. Gubía is with the Department of Electrical and Electronic Engineering and the Institute of Smart Cities, Public University of Navarre, 31006, Navarre, Spain (e-mail: uge@unavarra.es).

J. López is with the Department of Electrical and Electronic Engineering and the Institute of Smart Cities, Public University of Navarre, 31006, Navarre, Spain (e-mail: jesus.lopez@unavarra.es).

resistor is negative, the system will become unstable. This reduces the stability region to $f_s/6$, f_s being the sampling frequency. Several AD strategies have been proposed to extend this stability range. The computation delay can be reduced by shifting the capacitor current sampling instant towards the PWM reference update instant [15], or a lead compensator can be included in the feedback path in order to mitigate the impact of this delay [16]. The critical resonance frequency is extended to $f_s/4$ in [17] by modifying the transfer function that multiplies the capacitor current in the feedback loop. In [18] a recursive infinite impulse response digital filter is included in the feedback path in order to extend the system critical frequency to $0.45f_s$, whereas in [19] a quasi-integral element is employed to obtain a virtual positive resistor until half of the sampling frequency, $f_s/2$. In [20], the capacitor current is fed back through a PI, extending the stability range up to almost the Nyquist frequency, which improves the robustness against grid impedance variations. However, the range of possible resonance frequencies is bounded by the short circuit ratio (SCR) limits at the point of common coupling (PCC). Thus, extending the range where the virtual resistor is positive might not be the most interesting strategy. Instead, we could try to maximize the damping in the range of resonance frequencies by making the virtual resistance dominant against the reactance in this range.

Some works have been published that discuss AD strategies for DFIG wind turbines, yet none of them explores the capacitor current feedback AD. The DFIG system impedance can be reshaped, emulating a virtual impedance in series with the rotor winding or the GSC inductor, by means of the RSC or the GSC current feedback. With this purpose, a resonant controller can be used to reshape the frequency response only at the resonance frequency [21]. As an alternative, in [22] the damping controllers include a Chevyshev filter and a negative second order differential element. A stator voltage feedforward controller can also be employed to introduce a virtual impedance for the stator current controlled DFIG [23]. The controller includes a low-pass filter to limit the frequency range at which it actuates, and a lead-lag component to modify the phase of the DFIG impedance. However, all these strategies focus on mitigating the high-frequency resonance caused by the interaction of the DFIG system with the parallel compensated weak network, assuming that the internal resonance of the *LCL* filter is stable, or even considering a simple *L* filter [23].

Nevertheless, the *LCL* filter within the DFIG energy conversion system interacts with the impedance of the machine, the converter control and the grid, hence it must be precisely studied and specific AD strategies should be designed to stabilize it. As it is seen in Fig. 1, the stator of the generator is connected to the *LCL* filter capacitor. Therefore, the range of possible *LCL* resonance frequencies is modified by the DFIG impedance [24], which needs to be taken into account to calculate it. Moreover, the control loops of the GSC and the RSC interact with each other since they are connected in parallel to the grid through different impedances. This interaction must be modeled, as demonstrated in this paper, to properly evaluate the system stability and design effective AD strategies. This paper proposes a capacitor current feedback AD that considers the special features of DFIG wind turbines. Since the range of possible resonance frequencies is modified in this system, the strategies proposed so far, based on the capacitor current feedback, either cannot be applied directly because they increase instability, or do not maximize the damping provided in the actual resonance frequency range. The proposed strategy aims to maximize the damping in the range of resonance frequencies by the adjustment of the control delays. This method is shown to be effective and robust irrespective of the grid inductance.

The AD strategy can be implemented in either the GSC or the RSC, providing in both cases a similar damping to the *LCL* filter resonant poles. The suitability of the implementation in each converter is discussed in the paper. Finally, another contribution of the proposed strategy is that it can be applied in the GSC and the RSC at the same time in order to maximize the damping for a single value of grid inductance, which may be very helpful to comply with stringent grid codes that impose limits on the grid current harmonic content for a specific grid inductance [25]. This adjustment can be done thanks to the combined modeling of the GSC and the RSC control loops. The interaction between both converters, the DFIG system model and the proposed AD strategy are validated by experimental results obtained in a test bench.

II. System Modeling and Stability Analysis

A. System Description and Model

The configuration of a DFIG wind turbine is shown in Fig. 1. The back-to-back power converter that is connected to the rotor windings is formed by two converters, the rotor side converter and the grid side converter. The RSC controls the stator active and reactive power, whereas the GSC provides a stable DC-bus voltage. Both converters are connected in parallel, therefore both dynamics and control loops interact with each other, affecting the system stability.

All the system is connected to the medium voltage grid through a step up transformer at the PCC, therefore the transformer leakage inductance, L_t, is considered a part of the *LCL* harmonic filter. L_{pcc} is the inductance at the PCC, whose value depends on the grid SCR. L_{GSC} is the GSC output inductance and C_f is the filter capacitance.

In order to analyze the system stability, all the elements must be modeled in the same reference frame. Since DFIG wind turbines are normally controlled in the synchronous reference frame, *dq*, all the elements are modeled in this reference frame, using 2x2 impedance matrices and transfer function matrices with cross-coupling terms, which leads to a MIMO system. In this paper, impedance matrices and transfer function matrices are defined between brackets. Vectors are denoted by capital letters with the subscript *dq* to indicate the reference frame in which they are expressed.

1) DFIG Model: The equations of a doubly-fed induction generator are the following

$$V_{Sdq} = [Z_{L_m}]_{\omega_0} I_{Rdq} + ([Z_{L_m}]_{\omega_0} + [Z_{RL_{Sl}}]_{\omega_0}) I_{Sdq} \quad (1)$$

This article has been accepted for publication in a future issue of this journal, but has not been fully edited. Content may change prior to final publication. Citation information: DOI 10.1109/TPEL.2021.3089282, IEEE Transactions on Power Electronics

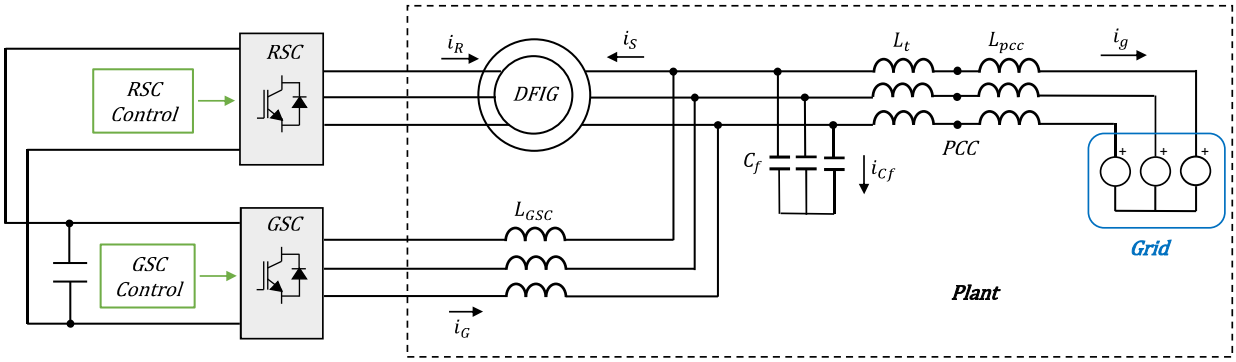

Fig. 1. DFIG wind turbine with an *LCL* filter connected to the grid.

$$V_{Rdq} = ([Z_{L_m}]_{\omega_R} + [Z_{RL_{Rl}}]_{\omega_R})I_{Rdq} + [Z_{L_m}]_{\omega_R} I_{Sdq}, \quad (2)$$

where the subscript S and R indicate whether the electrical variables belong to the stator or rotor winding. The impedance matrices $[Z_{L_m}]_\omega$, $[Z_{RL_{Sl}}]_{\omega_0}$ and $[Z_{RL_{Rl}}]_{\omega_R}$ are defined as

$$[Z_{L_m}]_\omega = \begin{bmatrix} L_m s & -L_m\omega \\ L_m\omega & L_m s \end{bmatrix}, \quad (3)$$

$$[Z_{RL_{Sl}}]_{\omega_0} = \begin{bmatrix} R_S + L_{Sl}s & -L_{Sl}\omega_0 \\ L_{Sl}\omega_0 & R_S + L_{Sl}s \end{bmatrix}, \quad (4)$$

$$[Z_{RL_{Rl}}]_{\omega_R} = \begin{bmatrix} R_R + L_{Rl}s & -L_{Rl}\omega_R \\ L_{Rl}\omega_R & R_R + L_{Rl}s \end{bmatrix}, \quad (5)$$

where R_R and R_S are the windings series resistances, L_m is the magnetizing inductance, L_{Sl} is the stator leakage inductance and L_{Rl} is the rotor leakage inductance. All the parameters of the DFIG machine are referred to the stator. The subscript outside the brackets indicates the angular speed of the cross-coupling terms. ω_0 is the angular speed of the *dq* axis, which is equal to the grid fundamental speed. $\omega_R = \omega_0 - \omega_m$, ω_m being the rotor electrical angular speed. Note that $[Z_{L_m}]_\omega$ is evaluated at ω_0 in (1) and ω_R in (2). The stator impedance matrix, $[Z_{RL_S}]_{\omega_0}$, is the sum of $[Z_{RL_{Sl}}]_{\omega_0}$ and $[Z_{L_m}]_\omega$ evaluated at ω_0. Similarly, $[Z_{RL_{Rl}}]_{\omega_R}$ and $[Z_{L_m}]_{\omega_R}$ can be combined into $[Z_{RL_R}]_{\omega_R}$.

The stator voltage is equal to the *LCL* filter capacitor voltage

$$V_{Sdq} = V_{Cfdq}. \quad (6)$$

2) LCL Harmonic Filter Model: The impedance matrices of the *LCL* filter components are the following

$$[Z_{RL_{GSC}}]_{\omega_0} = \begin{bmatrix} R_{GSC} + L_{GSC}s & -L_{GSC}\omega_0 \\ L_{GSC}\omega_0 & R_{GSC} + L_{GSC}s \end{bmatrix}, \quad (7)$$

$$[Z_{Cf}]_{\omega_0} = \begin{bmatrix} R_{Cf} + \frac{s}{C_f(s^2+\omega_0^2)} & \frac{\omega_0}{C_f(s^2+\omega_0^2)} \\ -\frac{\omega_0}{C_f(s^2+\omega_0^2)} & R_{Cf} + \frac{s}{C_f(s^2+\omega_0^2)} \end{bmatrix}, \quad (8)$$

$$[Z_{RL_g}]_{\omega_0} = \begin{bmatrix} R_g + L_g s & -L_g\omega_0 \\ L_g\omega_0 & R_g + L_g s \end{bmatrix}, \quad (9)$$

where R_{GSC} is the GSC inductor series resistance, R_{Cf} is the filter capacitor series resistance, R_g is the grid inductor series resistance and $L_g = L_t + L_{pcc}$.

The current through the GSC inductor I_{Gdq} is given by

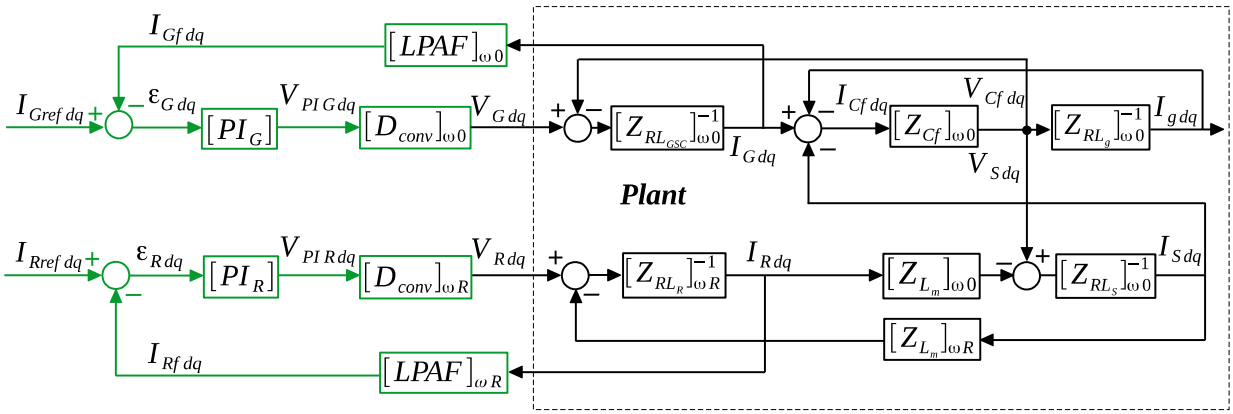

Fig. 2. Block diagram of the GSC and RSC current control loop.

$$I_{Gdq} = [Z_{RL_{GSC}}]_{\omega_0}^{-1} (V_{Gdq} - V_{Cfdq}), \quad (10)$$

where V_{Gdq} is the voltage imposed by the GSC. The filter capacitor voltage, V_{Cfdq}, is given by

$$V_{Cfdq} = [Z_{Cf}]_{\omega_0} I_{Cfdq}. \quad (11)$$

The grid current I_{gdq} is defined as follows

$$I_{gdq} = [Z_{RL_g}]_{\omega_0}^{-1} V_{Cfdq}. \quad (12)$$

Finally, the current through the filter capacitor I_{Cfdq} is given by

$$I_{Cfdq} = I_{Gdq} - I_{gdq} - I_{Sdq}. \quad (13)$$

3) Plant Model: Equations (1), (2), (6), (10), (11), (12) and (13) are combined to obtain the complete plant model that relates the GSC and the RSC currents, I_{Gdq} and I_{Rdq}, to the voltages imposed by each converter, V_{Gdq} and V_{Rdq}. As a result, a 4x4 transfer function matrix, $[Plant]_{4x4}$, is obtained

$$\begin{Bmatrix} I_{Gdq} \\ I_{Rdq} \end{Bmatrix} = [Plant]_{4x4} \begin{Bmatrix} V_{Gdq} \\ V_{Rdq} \end{Bmatrix}. \quad (14)$$

4) GSC and RSC current control loop model: The GSC and the RSC are controlled as current sources. The block diagram of the current control loop of each power converter appears in Fig. 2, demonstrating the interaction between the two converters as both of them act on the same plant, which is formed by the DFIG machine and the *LCL* filter.

The GSC and the RSC currents are controlled using a PI regulator in the synchronous reference frame *dq*, filtering the currents with a low pass analog filter, $LPAF(s) = 1/(\tau s+1)$, used to filter noise at the switching frequency. The cutoff frequency is $f_s/4$. The control is implemented in a digital signal processor (DSP), sampling the variables once per switching period (symmetrical regular sampling). $D_{conv}(s)$ models the computational delay of the DSP and the effect of the PWM, approximated by a zero order hold. The total delay of 1.5 sample periods is modeled using the fourth order approximation given in [11], in order to obtain an accurate representation at high frequencies.

There are three reference frames in the system. The elements of the GSC control loop, i.e. $LPAF(s)$ and $D_{conv}(s)$, are defined in the stator stationary reference frame, $\alpha\beta_s$; and the elements of the RSC control loop are defined in the rotor stationary reference frame, $\alpha\beta_m$, which rotates at the rotor angular speed ω_m. The system is controlled in the synchronous reference frame, *dq*, so in order to perform the stability analysis, all the elements are modeled in *dq*. For that, each element is defined in its corresponding reference frame, where there are no cross-coupling terms, and then a rotation is performed using the transformation detailed in [26]. For example, considering the transfer function $D_{conv}(s)$, the transformation from the stationary to the synchronous reference frame is given by

$$[D_{conv}]_\omega = \frac{1}{2} \begin{bmatrix} D_{conv1}(s) & D_{conv2}(s) \\ -D_{conv2}(s) & D_{conv1}(s) \end{bmatrix}, \quad (15)$$

where $D_{conv1}(s) = D_{conv}(s + j\omega) + D_{conv}(s - j\omega)$ and $D_{conv2}(s) = jD_{conv}(s + j\omega) - jD_{conv}(s - j\omega)$.

The speed used to perform the rotation, ω, depends on the reference frame in which each element is defined. The rotation of the elements defined in the $\alpha\beta_s$ reference frame is made using the grid fundamental speed ω_0, whereas the rotation of the elements defined in the $\alpha\beta_m$ reference frame is made using ω_R. In the block diagram of Fig. 2, the subscript outside the brackets of each transfer function matrix indicates the angular speed at which the element is rotated. This way, different transfer functions are obtained for the elements of the control loop of each converter.

The last element of the current control loop is the PI regulator, which is defined in *dq* axis as shown in (16). There are two PI controllers, $[PI_G]$ and $[PI_R]$, one for each converter, which have different parameters: K_{pG} and T_{nG} for the GSC; and K_{pR} and T_{nR} for the RSC.

$$[PI] = \begin{bmatrix} K_p \frac{T_n s+1}{T_n s} & 0 \\ 0 & K_p \frac{T_n s+1}{T_n s} \end{bmatrix}. \quad (16)$$

All the impedance matrices and transfer function matrices that model the elements of the system are symmetric matrices. The system plant is modeled by a 4x4 transfer function matrix, $[Plant]_{4x4}$, whereas the elements of the current control loops are modeled by 2x2 transfer function matrices, so they must be expanded to 4x4 matrices. For example, the 4x4 transfer matrix of the GSC PI regulator, $[PI_G]_{4x4}$, is given by

$$[PI_G]_{4x4} = \left[\begin{array}{c|c} [PI_G] & [0_2] \\ \hline [0_2] & [0_2] \end{array}\right], \quad (17)$$

where $[0_2]$ is the second order zero matrix.

From the plant model and the expanded models of the elements of the current control loops, the open-loop transfer function matrix $[H_{ol}]_{4x4}$ can be obtained. This 4x4 transfer matrix consists of four 2x2 matrices, each of them having two subscripts. The first one refers to the output, whereas the second one refers to the input. In both cases, G stands for the GSC and R for the RSC.

$$[H_{ol}]_{4x4} = \left[\begin{array}{c|c} [H_{GG}] & [H_{GR}] \\ \hline [H_{RG}] & [H_{RR}] \end{array}\right]. \quad (18)$$

This matrix relates the GSC and the RSC currents to their current tracking errors

$$\begin{Bmatrix} I_{Gfdq} \\ I_{Rfdq} \end{Bmatrix} = \left[\begin{array}{c|c} [H_{GG}] & [H_{GR}] \\ \hline [H_{RG}] & [H_{RR}] \end{array}\right] \begin{Bmatrix} \varepsilon_{Gdq} \\ \varepsilon_{Rdq} \end{Bmatrix}. \quad (19)$$

B. Influence of the DFIG machine on the LCL filter resonance frequency

The resonance frequency of an *LCL* filter depends on the grid SCR. The variability of the SCR can lead to a wide range of possible resonance frequencies and the system should be stable in every case. Therefore, the full range of possible

This article has been accepted for publication in a future issue of this journal, but has not been fully edited. Content may change prior to final publication. Citation information: DOI 10.1109/TPEL.2021.3089282, IEEE Transactions on Power Electronics

resonance frequencies is obtained taking as the lower limit the value corresponding to a SCR of zero and, as the upper limit, the value calculated for a SCR of infinity. The limits for an *LCL* filter without the DFIG are given by

$$frl_{LCL} = \frac{1}{2\pi}\sqrt{\frac{1}{L_{GSC}C_f}} \tag{20}$$

$$frh_{LCL} = \frac{1}{2\pi}\sqrt{\frac{L_{GSC}+L_t}{L_{GSC}L_tC_f}}. \tag{21}$$

In a DFIG system the impedance of the machine interacts with the impedance of the *LCL* filter, modifying the resonance frequency. The complete model of the DFIG generator that has been derived before is too complex to study this interaction. Thus, the model is simplified neglecting the magnetizing inductance, L_m, which offers a high reactance at high frequencies and may have a low influence on the *LCL* filter resonance. This way, the block diagram of the plant in Fig. 3 is obtained.

The equation of the doubly-fed induction generator is now

$$I_{Rdq} \approx -I_{Sdq} = [Z_{DFIG}]^{-1}\left(V_{Rdq} - V_{Sdq}\right), \tag{22}$$

where $[Z_{DFIG}] = [Z_{RL_{Sl}}]_{\omega_0} + [Z_{RL_{Rl}}]_{\omega_R}$.

Fig. 4 shows the comparison between the frequency response of the transfer function correlating the grid current I_{gdq} and the rotor voltage V_{Rdq}, using the complete plant model (blue curve) versus the simplified model (red curve) that reduces the DFIG model to the stator and rotor leakage inductances. These Bode diagrams are represented for the system parameters reported in Table II. Since the impedance matrices are symmetric matrices, and the resulting 2x2 matrix that models the dynamics between I_{gdq} and V_{Rdq} is also symmetric for both models, two Bode diagrams are sufficient to analyze the plant dynamics. At high frequencies where the *LCL* filter resonance occurs, the diagonal term is dominant over the anti-diagonal term. By observing Fig. 4 (a), it can be deduced that at the lower end of the range, the dominant response is inductive, then the magnitude increases at the resonance frequency and, at the higher end of the range, the system has a capacitive response. In *dq* axis two resonance peaks appear at $\pm f_0$ of the real value of the resonance frequency, f_0 being the grid fundamental frequency equal to 50 Hz. In both Fig. 4 (a) and (b), the response of the plant with the simplified model of the DFIG is very similar to the response using the complete model within the range of resonance frequencies. Thus, the magnetizing inductance does not influence the dynamics of the system at high frequencies

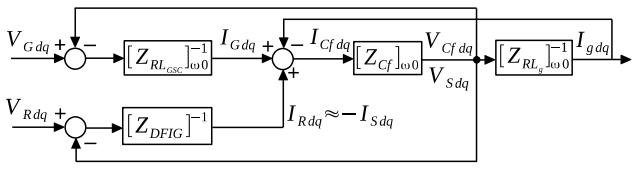

Fig. 3. Block diagram of the plant with the simplified model of the DFIG machine.

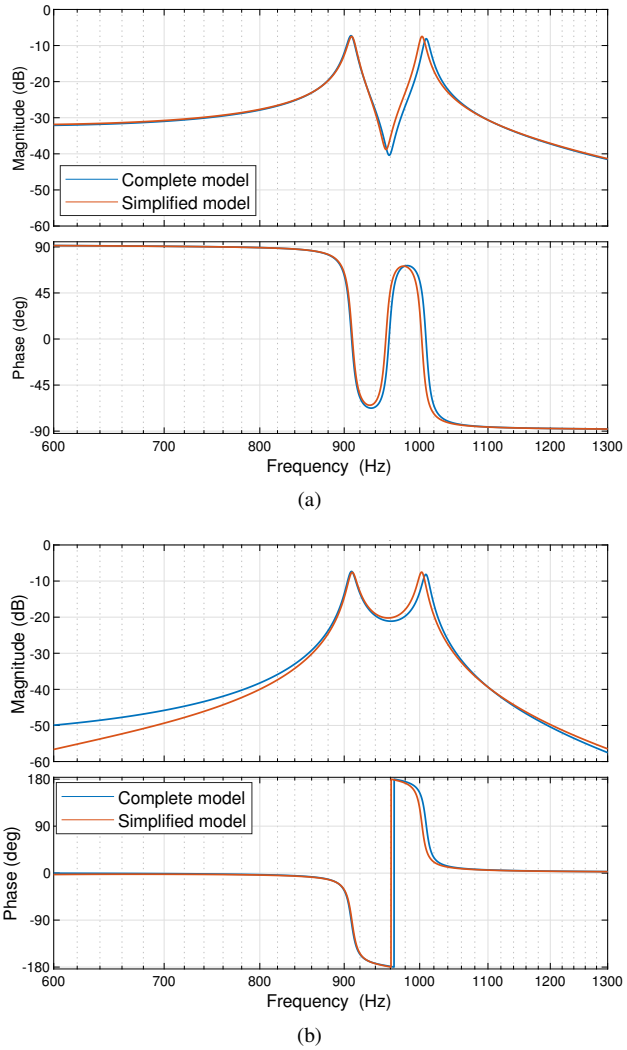

(a)

(b)

Fig. 4. Frequency response of the transfer function correlating the grid current I_{gdq} and the rotor voltage V_{Rdq} using the complete plant model and the simplified model, diagonal term (a) and anti-diagonal term (b).

and the simplification is validated in the resonance frequency range.

Neglecting the magnetizing inductance, L_m, the limits of the resonance frequency range for the DFIG system are given by

$$frl_{DFIG} = \frac{1}{2\pi}\sqrt{\frac{L_{GSC}+L_l}{L_{GSC}L_lC_f}} \tag{23}$$

$$frh_{DFIG} = \frac{1}{2\pi}\sqrt{\frac{L_{GSC}L_t + L_{GSC}L_l + L_lL_t}{L_{GSC}L_lL_tC_f}}, \tag{24}$$

where $L_l = L_{Sl} + L_{Rl}$.

TABLE I
RESONANCE FREQUENCY RANGE LIMITS

Configuration	frl	frh
LCL	$0.13f_s$ (516 Hz)	$0.26f_s$ (1024 Hz)
DFIG + LCL	$0.17f_s$ (686 Hz)	$0.28f_s$ (1120 Hz)

This article has been accepted for publication in a future issue of this journal, but has not been fully edited. Content may change prior to final publication. Citation information: DOI 10.1109/TPEL.2021.3089282, IEEE Transactions on Power Electronics

TABLE II
SYSTEM PARAMETERS

Parameter	Value
DFIG S = 5 kVA, U = 230 V	
Rotor resistance	0.071 p.u.
Rotor leakage inductance	0.122 p.u.
Stator resistance	0.059 p.u.
Stator leakage inductance	0.128 p.u.
Magnetizing inductance	2.375 p.u.
Power converters	
Switching frequency	4 kHz
Sampling frequency	4 kHz
GSC inductor	0.192 p.u.
GSC inductor series resistance	0.028 p.u.
Filter capacitor	0.049 p.u.
Filter capacitor series resistance	0.001 p.u.
Transformer inductor	0.065 p.u.
Transformer inductor series resistance	0.010 p.u.
Control parameters	
GSC PI proportional gain	2
GSC PI integration time	0.01
RSC PI proportional gain	2.8
RSC PI integration time	0.01
GSC, RSC current LPAF time constant	150.10^{-6}
Capacitor current LPAF time constant	47.10^{-6}

The value of these limits are given in Table I as a ratio with respect to f_s, as well as the absolute value in Hz. The limits are calculated for the system parameters given in Table II. In the DFIG system, the total value of the inductance decreases, compared to an *LCL* filter, and the resonance frequency shifts towards higher frequencies. Besides, the range of possible resonance frequencies becomes narrower. It can be concluded that the interaction between the machine impedance and the *LCL* filter impedance must be considered in order to calculate the system resonance frequency. Otherwise, the AD strategy would be adjusted for the wrong frequencies and the resonant poles would not be properly damped.

C. Stability Analysis

In the previous subsection, the interaction between the DFIG machine and the *LCL* harmonic filter impedances has been analyzed. Now, the system stability and the interaction between the GSC and the RSC control loops are studied.

The stability of a MIMO system can be evaluated through the open-loop matrix eigenvalues' analysis. The controllers of the GSC and the RSC are designed to achieve the desired dynamic performance in each converter. Thus, the GSC and the RSC open-loop transfer matrices, $[H_{Gol}]$ and $[H_{Rol}]$, which are 2x2 matrices, are computed from $[H_{ol}]_{4x4}$ in (19). If the interaction between both converters is neglected, $[H_{Gol}]$, relating ε_{Gdq} to I_{Gfdq}, is computed imposing $\varepsilon_{Rdq} = 0$; and $[H_{Rol}]$, relating ε_{Rdq} to I_{Rfdq}, is computed making $\varepsilon_{Gdq} = 0$. This way, $[H_{Gol}] = [H_{GG}]$ and $[H_{Rol}] = [H_{RR}]$. The expression for their eigenvalues is

$$\lambda_{1,2} = H_{ol1} \pm jH_{ol2}, \tag{25}$$

where H_{ol1} and H_{ol2} are the diagonal and anti-diagonal terms of the matrices.

The MIMO Generalized Bode Criterion [27] is applied to calculate the number of closed-loop unstable poles, Z, by analyzing the Bode diagram of the open-loop eigenvalues. This criterion is expressed as

$$Z = P - [2(C^+ - C^-) + C_0], \tag{26}$$

where P is the number of open-loop unstable poles, C^+ is the number of $\pm m180$ degree crossings with positive magnitude and increasing phase (m odd integer) only at positive frequencies in the Bode diagram of all the system open-loop eigenvalues, C^- is the number of crossings with decreasing phase and C_0 is the number of crossings at 0 Hz.

The stability analysis is done with the complete plant model derived in subsection II-A. The system parameters are reported in Table II. The rotor speed does not influence the impedance of the DFIG system in the range of possible resonance frequencies [28], therefore a slip equal to -0.25 is selected to perform this analysis, where $slip = \frac{\omega_R}{\omega_0}$.

The PI controllers design is based on the method proposed in [27]. Following this design procedure, it can be verified that both eigenvalues of the GSC have a crossing at 0 Hz, thus $C_0 = -2$, whereas the RSC has no crossings, so $C_0 = 0$. This way, for the GSC to be stable a $\pm m180$ degree crossing with positive magnitude and increasing phase needs to be introduced in one eigenvalue according to (26). In the case of the RSC, no crossings have to be introduced. The PI parameters K_p and T_n for both converters are computed to achieve the desired dynamics. A controller bandwidth of 90 Hz is selected for the GSC and 60 Hz for the RSC, with a minimum phase margin of 30 degrees for a SCR of 20. The resulting PI parameters appear in Table II.

The eigenvalues Bode diagram of $[H_{Gol}]$ and $[H_{Rol}]$ for a SCR of 20 are represented in Fig. 5. In the case of the GSC (blue), the 180 degree crossing with positive magnitude and increasing phase is produced, thus $C^+ = 1$. Since $C_0 = -2$ and there are no open-loop unstable poles, the number of closed-loop unstable poles is zero and the system is stable ($Z = 0$ in (26)). For the RSC (red), there are no crossings with $\pm m180$ degrees and positive magnitude, nor open-loop

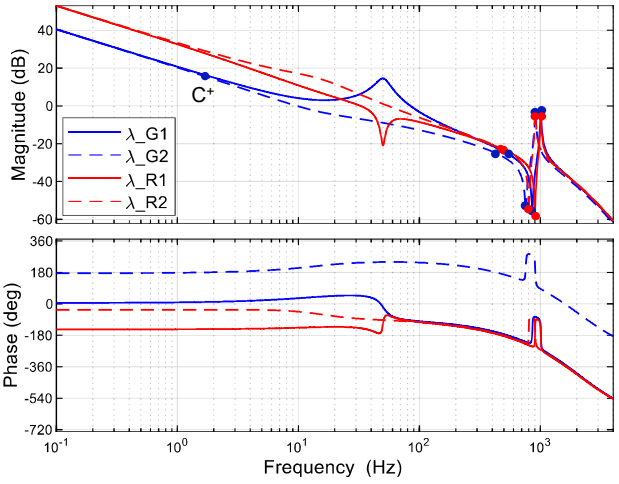

Fig. 5. Eigenvalues Bode diagram of the GSC and the RSC open-loop transfer matrix neglecting the interaction between both converters, for a SCR of 20.

This article has been accepted for publication in a future issue of this journal, but has not been fully edited. Content may change prior to final publication. Citation information: DOI 10.1109/TPEL.2021.3089282, IEEE Transactions on Power Electronics

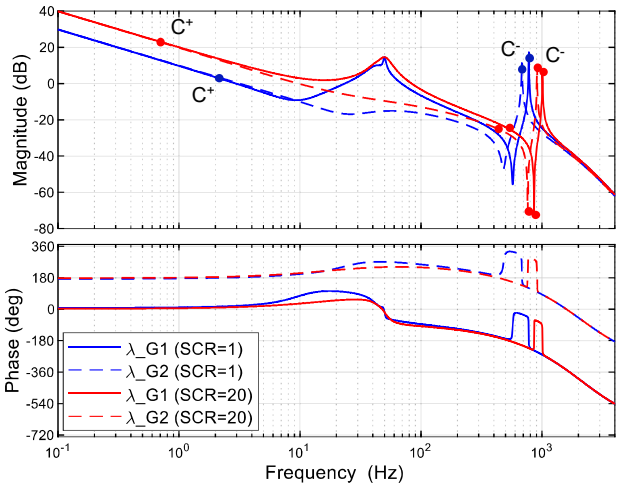

Fig. 6. Eigenvalues Bode diagram of the GSC open-loop transfer matrix considering the interaction between the GSC and the RSC.

unstable poles, so $Z = 0$ and the closed-loop system is also stable. It is demonstrated that both control loops are stable when the converters do not interact with each other.

However, in the complete DFIG system, the GSC and the RSC are connected in parallel to the grid, so there is an interaction between both control loops. Now, the system stability is analyzed taking into account this interaction. In this case, $[H_{Gol}]$ is calculated making $I_{Rrefdq} = 0$ and thus, $\varepsilon_{Rdq} = -I_{Rfdq}$. Equivalently, $[H_{Rol}]$ is obtained imposing $I_{Grefdq} = 0$, which means $\varepsilon_{Gdq} = -I_{Gfdq}$. These two matrices are given by

$$[H_{Gol}] = [H_{GG}] - [H_{GR}]\left([I_2] + [H_{RR}]\right)^{-1}[H_{RG}] \quad (27)$$

$$[H_{Rol}] = [H_{RR}] - [H_{RG}]\left([I_2] + [H_{GG}]\right)^{-1}[H_{GR}], \quad (28)$$

where $[I_2]$ is the order two identity matrix.

Fig. 6 shows the eigenvalues of $[H_{Gol}]$, for a SCR of 1 and 20 and the PI parameters previously computed. For each SCR, there are two crossings at 0 Hz, one in each eigenvalue, thus $C_0 = -2$. There is one 180 degree crossing with positive magnitude and increasing phase, therefore $C^+ = 1$. Since there are no open-loop unstable poles, if there were no more crossings with ± 180 degrees, the system would be stable in both cases. However, the interaction between both converters tends to increase the magnitude in the Bode diagram, which introduces two crossings with decreasing phase at the resonance frequency for each SCR, so $C^- = 2$. As a consequence, there are 4 unstable closed-loop poles at this frequency for each SCR. The frequency of the unstable poles is within the range of possible resonance frequencies for the DFIG wind turbine that has been calculated in the previous subsection by means of (23) and (24).

It can be concluded that the interaction between the GSC and the RSC must be considered, as otherwise the stability analysis can lead to incorrect conclusions. Furthermore, the DFIG system is unstable due to the resonance of the *LCL* filter. Because of that, a damping strategy is needed.

III. Proposed Active Damping Strategy

A. Fundamentals of the Strategy

The proposed active damping method is based on the capacitor current feedback. As it is seen in Fig. 7 (a), the capacitor current is filtered using a low pass analog filter, modeled in *dq* axis by $[LPAF]_{\omega_0}$, to attenuate noise at the switching frequency. $[H_{ADG}]$ and $[H_{ADR}]$ are the proposed AD transfer matrices, which are defined in *dq* axis, and k_G and k_R are the proportional gains. By operating in the block diagram of Fig. 7 (a), it can be deduced that the effect of this control action from each converter is equivalent to implementing a virtual impedance in parallel with the filter capacitor. The input node is shifted from the capacitor current, I_{Cfdq}, to the capacitor voltage, V_{Cfdq}; and the AD action is shifted from the output of the PI controllers to before the filter capacitor impedance matrix, $[Z_{Cf}]_{\omega_0}$. These virtual impedances are represented in Fig. 7 (b) by the dashed red blocks. The expression of the virtual impedance matrix in *dq* coordinates implemented by each converter is given by

$$[Z_{ADG}] = \\ = \left([Z_{Cf}]^{-1}_{\omega_0}[LPAF]_{\omega_0}[H_{ADG}]k_G[D_{conv}]_{\omega_0}[Z_{RL_{GSC}}]^{-1}_{\omega_0}\right)^{-1} \quad (29)$$

$$[Z_{ADR}] = \\ = \left([Z_{Cf}]^{-1}_{\omega_0}[LPAF]_{\omega_0}[H_{ADR}]k_R[D_{conv}]_{\omega_R}[Z_{DFIG}]^{-1}\right)^{-1}. \quad (30)$$

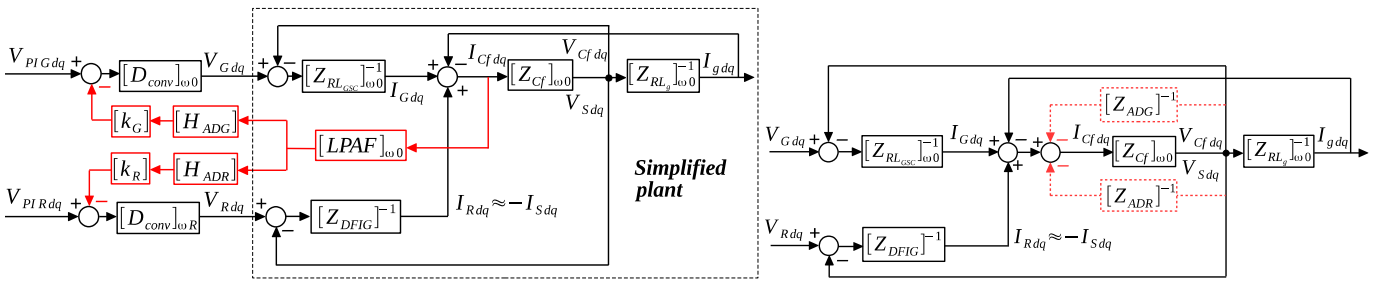

Fig. 7. Block diagram of the simplified plant and the proposed capacitor current feedback active damping (a) and equivalent virtual impedance (b).

This article has been accepted for publication in a future issue of this journal, but has not been fully edited. Content may change prior to final publication. Citation information: DOI 10.1109/TPEL.2021.3089282, IEEE Transactions on Power Electronics

All the terms in (29) and (30) are symmetric matrices, so the virtual impedance matrices are also symmetric. The magnitude of the diagonal terms is 6 times greater than the magnitude of the anti-diagonal terms within the range of possible resonance frequencies. Therefore, the anti-diagonal terms can be neglected when designing the AD strategy, so that the virtual impedance matrices become diagonal matrices. As a result, the AD transfer matrices, $[H_{ADG}]$ and $[H_{ADR}]$, are diagonal matrices, whose diagonal terms are $H_{ADG1}(s)$ and $H_{ADR1}(s)$, respectively. This way, the AD feedback is the same in both d and q axis, so only one axis can be considered to adjust the AD strategy. The expressions of the virtual impedances in one axis are given by

$$Z_{ADG1}(s) = \frac{L_{GSC}}{C_f k_G H_{ADG1}(s) D_{conv1}(s) LPAF_1(s)} \quad (31)$$

$$Z_{ADR1}(s) = \frac{L_l}{C_f k_R H_{ADR1}(s) D_{conv1}(s) LPAF_1(s)}. \quad (32)$$

The resistive component of the virtual impedance is related to the cosine of the phase of $Z_{ADG1}(s)$, which is shown in Fig. 8, against frequency. $Z_{ADG1}(s)$ is chosen as an example but the same reasoning can be done by studying the phase of $Z_{ADR1}(s)$. Initially, without any AD action, the lag is given by $D_{conv1}(s)$ and $LPAF_1(s)$ (dashed line). In this case, the resistive component in the resonance frequency range is dominated by the reactance, which does not provide enough damping to the system resonant poles. Even at low SCRs, the AD action would have a destabilizing effect if the sign of the emulated virtual resistance changes.

Our objective is to adjust the phase of the virtual impedance so that it has a dominant resistive behavior in the range of possible resonance frequencies in order to maximize the damping of the system resonant poles. For that purpose, the transfer functions $H_{ADG1}(s)$ and $H_{ADR1}(s)$ include a pure delay of y sample periods, e^{-syT_s}, where T_s is the sampling period. A different delay can be adjusted for the GSC and the RSC, y_G and y_R, respectively. Furthermore, the AD should only actuate in the resonance frequency range, for this reason the AD action is filtered. The inner AD loop already includes a low pass analog filter, thus, an additional first order high pass digital filter, $HPDF(s)$, is needed. It filters the fundamental component, which is seen at 0 Hz in the *dq* reference frame, to reduce the applied AD action. Therefore, the filter cutoff frequency is 100 Hz, providing an attenuation of -60 dB at 0 Hz.

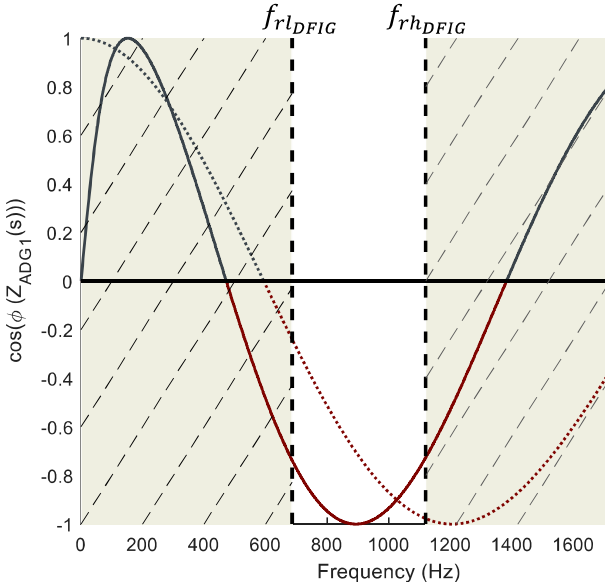

Fig. 8. Cosine of the phase of the virtual impedance versus frequency without adjusting the delay of the AD feedback loop (dashed line) and with the delay adjusted (continuous line).

The general expression for $H_{AD1}(s)$ is

$$H_{AD1}(s) = HPDF(s)e^{-syT_s}. \quad (33)$$

By making (31) equal to (32), the same virtual impedance can be emulated with both converters. The only elements that are different in both virtual impedances are the AD transfer functions, $H_{ADG1}(s)$ and $H_{ADR1}(s)$, the proportional gains, k_G and k_R, and the inductances, L_{GSC} and L_l. $HPDF(s)$ is the same in both transfer functions, so if the same delay, y_G and y_R, is adjusted in both converters, $H_{ADG1}(s)$ and $H_{ADR1}(s)$ would be identical. Thus, in order to obtain the same virtual impedance with both converters, the relation between the gains, k_G and k_R, must satisfy the following expression

$$\frac{k_G}{k_R} = \frac{L_{GSC}}{L_l}. \quad (34)$$

B. Active Damping Implementation in the GSC

In (31) the only elements that need to be adjusted are the gain k_G and and the delay y_G. First, the required delay y_G is calculated to emulate a pure resistor at the central resonance frequency, $f_{rc} = (frl_{DFIG} + frh_{DFIG})/2$, in order to ensure a robust damping of the system resonant poles regardless of the SCR. For that purpose, the phase of the virtual impedance $Z_{ADG1}(s)$ at f_{rc} should be equal to π, as expressed in (35). In this case, the required delay is $y_G = 0.617$.

$$\phi(Z_{ADG1}(j\omega_{rc})) = (2n+1)\pi$$
$$= -\phi(HPDF(j\omega_{rc})e^{-j\omega_{rc}y_G T_s} D_{conv1}(j\omega_{rc}) LPAF_1(j\omega_{rc})) \quad (35)$$

for $n = 0, 1, 2...$

Fig. 8 shows the resistive component of the virtual impedance $Z_{ADG1}(s)$ once the delay of y_G sample periods is adjusted (continuous line). Now, greater resistive behavior is achieved throughout the whole resonance frequency range, maximizing the damping. A negative resistor is emulated with this strategy, thus the inner AD loop becomes a capacitor current positive feedback.

Finally, the value of the gain k_G is determined. To that end, the eigenvalues of the inner AD open-loop transfer matrix are represented first, in Fig. 9. There are no unstable open-loop poles in the inner AD loop, therefore, considering (26), there should be no $\pm m180$ degree crossings with positive magnitude

This article has been accepted for publication in a future issue of this journal, but has not been fully edited. Content may change prior to final publication. Citation information: DOI 10.1109/TPEL.2021.3089282, IEEE Transactions on Power Electronics

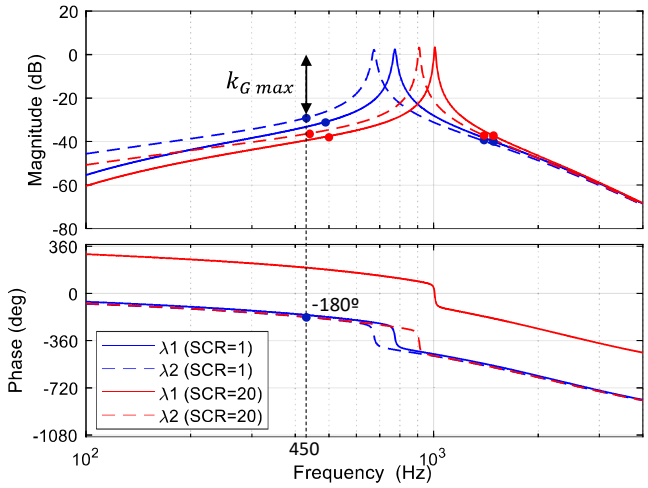

Fig. 9. Eigenvalues Bode diagram of the inner AD open-loop transfer matrix for two SCRs.

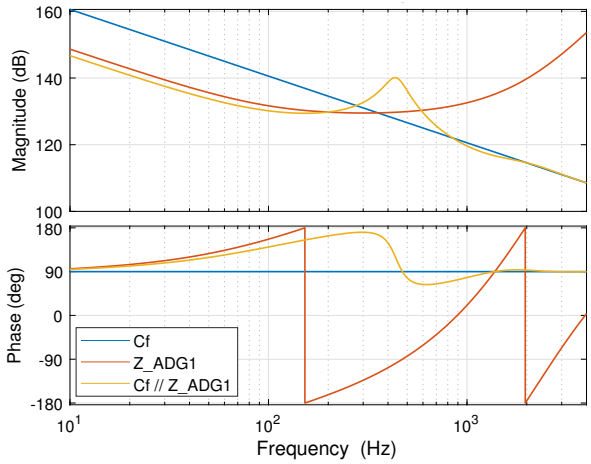

Fig. 11. Frequency response of the capacitor, the virtual impedance and the parallel connection of both of them.

for the AD feedback loop to be stable. The minimum gain margin for all SCRs is 29 dB. So, to guarantee the system stability in all cases, the maximum allowed value of k_G is 28. Otherwise a C^- crossing would be introduced at 450 Hz, and thus, there would be two unstable closed-loop poles at that frequency. Then, given this upper limit, the system closed-loop poles are studied for different values of k_G for a SCR of 20, as shown in Fig. 10, in order to determine the optimal value that provides the greatest damping to the system resonant poles. In this figure, the color of the zeros and poles becomes lighter as the gain increases. With a small gain, the system resonant poles are not sufficiently damped. As the gain increases, so does the damping, reaching the optimal value with $k_G = 16$. However, if the gain increases too much the system becomes unstable. In Fig. 10, the system poles with $k_G = 16$ are marked in red.

As it is observed, there are some poles around 450 Hz that are less damped as the value of the gain increases. This is due to the interaction between the implemented virtual impedance and the filter capacitor. Fig. 11 shows the frequency response of the capacitor, the virtual impedance, $Z_{ADG1}(s)$, and the parallel connection of both of them, for $k_G = 16$. As it is observed, the virtual impedance has inductive behavior around 450 Hz and resonates with the capacitor when both elements are connected in parallel. This new resonance tends to destabilize the system. In Fig. 10, the frequency of these poles varies slightly as the gain k_G changes because it modifies the value of the emulated virtual impedance. For this reason, the gain k_G has to be carefully selected, so that both the resonant poles and the medium frequency poles are properly damped.

Fig. 12 shows the closed-loop poles of the system for three different values of SCR that cover the whole range of possible resonance frequencies. As it is observed, the resonant poles, circled in the figure, are stabilized in all the cases thanks to the proposed active damping strategy.

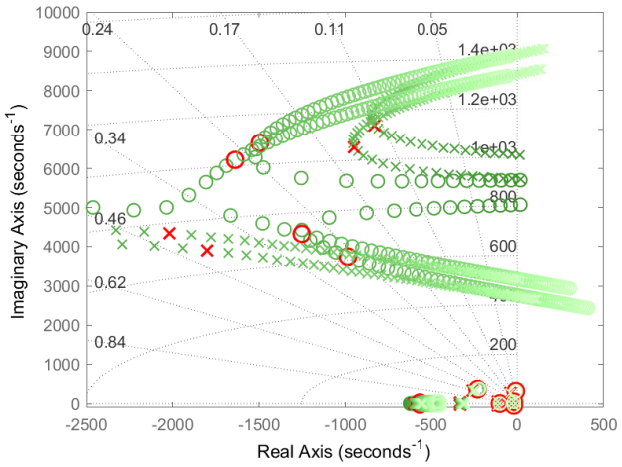

Fig. 10. Closed-loop poles of the system for different values of k_G for a SCR of 20.

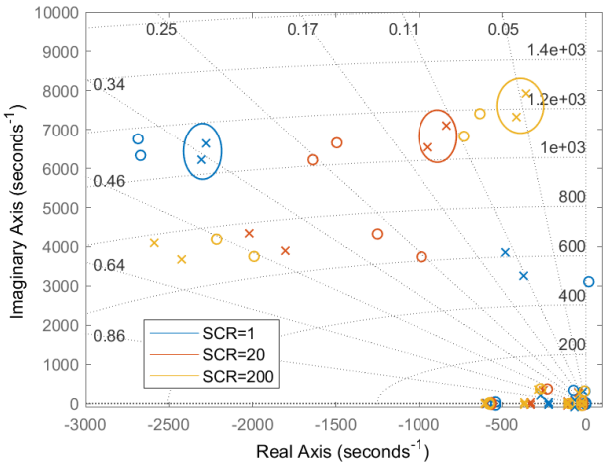

Fig. 12. Closed-loop poles of the system with the proposed AD implemented in the GSC for three SCRs.

This article has been accepted for publication in a future issue of this journal, but has not been fully edited. Content may change prior to final publication. Citation information: DOI 10.1109/TPEL.2021.3089282, IEEE Transactions on Power Electronics

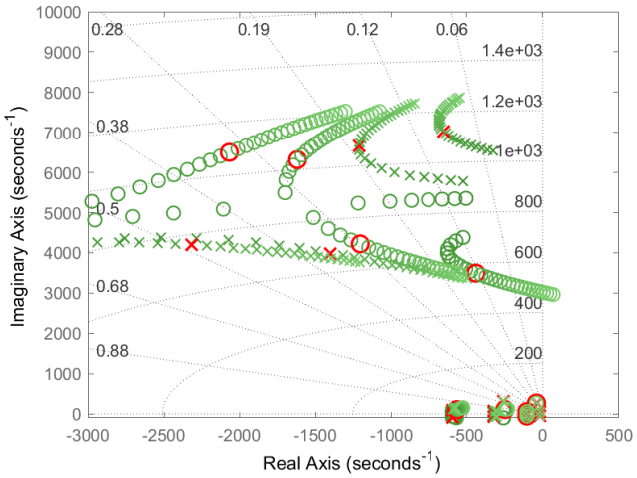

Fig. 13. Closed-loop poles of the system for different values of k_R for a SCR of 20.

C. Active Damping Implementation in the RSC

As for the GSC, the only elements that need to be adjusted in (32) are the gain k_R and the delay y_R. Again, a virtual resistor is emulated at the central resonance frequency, f_{rc}, in order to obtain a robust damping of the resonant poles for any SCR. Since both virtual impedances contain equal elements, the delay remains the same as before, $y_R = 0.617$. Considering that the delay does not change, (34) is used to calculate the optimal value of the gain k_R, which is 21.

The system closed-loop poles for a SCR equal to 20 are studied for different values of k_R, close to the calculated one, in order to verify whether it is the optimal value that provides the greatest damping. In Fig. 13, the closed-loop poles of the system for k_R between 10 and 40 are represented and the poles corresponding to $k_R = 21$ are marked in red. It is observed that the calculated value is very close to the optimal one, as expected. In Fig. 14, the closed-loop poles of the system for three SCRs are represented, with the AD strategy implemented in the RSC. As it is observed, the resonant poles, circled in the figure, are stabilized whether the converter is connected to weak or strong grids.

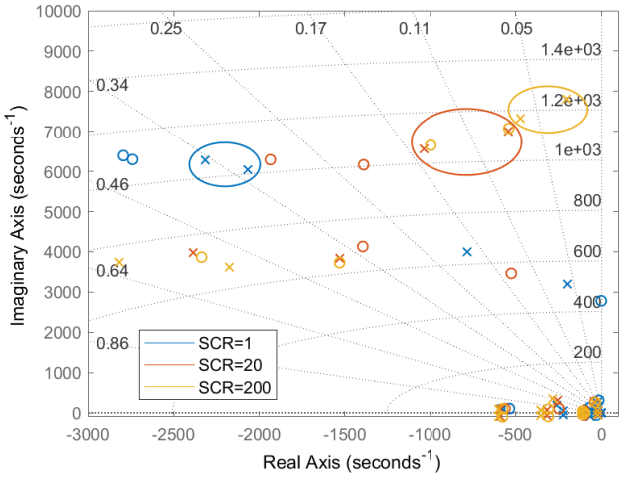

Fig. 14. Closed-loop poles of the system with the proposed AD implemented in the RSC for three SCRs.

It has been proved that the resonant poles of the DFIG wind turbine can be effectively damped applying the AD strategy in either of the two converters, which increases the flexibility of the control strategy. The main difference between the required AD action in each converter is due to the difference of the proportional gains, k_G and k_R. The higher the value of the gain, the higher the AD action. Therefore, the AD strategy can be implemented in the converter that is further from saturation. This way, the DC-bus voltage does not need to be increased in order to provide the additional action calculated by the AD feedback loop.

D. Combined Active Damping Implementation in the GSC and the RSC

In the previous subsections, it has been explained the adjustment of the AD strategy to obtain a robust damping of the resonant poles for the full range of possible resonance frequencies. However, during operation, the value of the grid SCR does not vary between zero and infinity. Normally, the strength of the grid to which the wind turbine is connected is known, hence the resonance frequency range is narrower and the AD can be adjusted to maximize the damping in this desired interval. Furthermore, the grid current harmonic content must comply with the limits imposed by grid codes, which often consider the value of the SCR at the PCC [25]. In this case, the damping could be maximized for that specific resonance frequency.

In order to do that, the usage of both converters, GSC and RSC, is proposed in this paper. The AD strategy is implemented in both converters simultaneously, properly adjusting the delay and the gain of each of them. We assume that the robust AD of the GSC is already adjusted as shown in subsection III-B, which stabilizes the resonant poles for every SCR. Then, the AD of the RSC is readjusted with the aim of providing more damping at the desired resonance frequency. In this case, the strategy is tuned for a SCR of 20, which corresponds to a resonance frequency of 956 Hz.

First, the closed-loop poles of the GSC control loop are analyzed after the AD strategy has been applied. The emulated virtual impedance has a real part and an imaginary part. The real part damps the resonant poles, whereas the imaginary part changes the resonance frequency. For that reason, the new frequency of the resonant poles for the SCR of 20 is 1100 Hz, as seen in Fig. 12, using the lines of constant frequency. Then, the AD of the RSC is adjusted considering that the resonant poles are already damped by the GSC. The RSC control loop sees the resonant poles at this new frequency. Thus, the delay y_R is calculated to obtain a pure virtual resistor at 1100 Hz, so that the damping is maximized at this frequency. In this case, $y_R = 0.204$, which is lower than in the previous adjustment for the RSC because the *LCL* filter resonance is shifted towards higher values by the virtual impedance $[Z_{ADG}]$. Finally, the value of the gain k_R has to be determined.

Fig. 15 shows the closed-loop poles of the system for different values of k_R and a SCR of 20, in green, considering

This article has been accepted for publication in a future issue of this journal, but has not been fully edited. Content may change prior to final publication. Citation information: DOI 10.1109/TPEL.2021.3089282, IEEE Transactions on Power Electronics

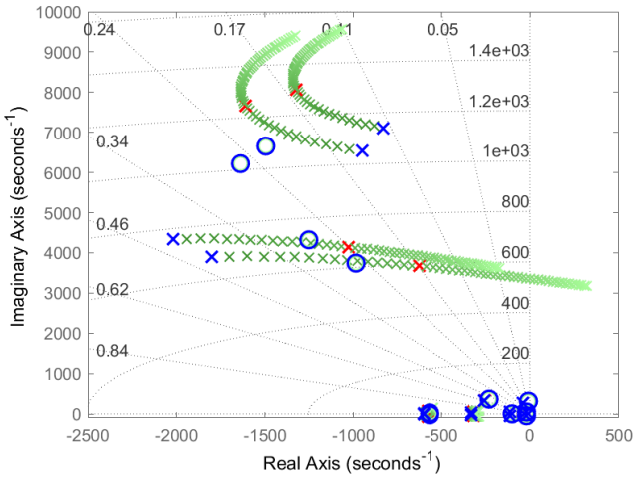

Fig. 15. Closed-loop poles of the system when the AD is only implemented in the GSC (blue) and when the AD is also implemented in the RSC for different values of k_R (green), for a SCR of 20.

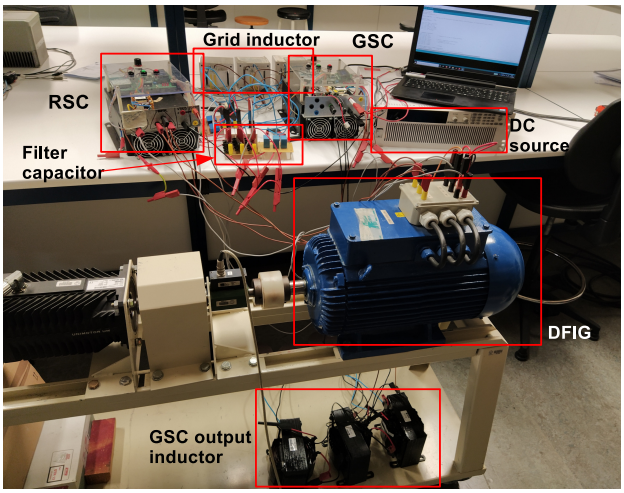

Fig. 16. Experimental setup of a DFIG wind turbine.

that the AD is already implemented in the GSC. In this case, the gain that provides the maximum damping is $k_R = 17$, which yields the closed-loop poles marked in red in the figure. The damping that is obtained in this case is $\xi = 0.16$, whereas the damping that is obtained when the AD is only applied in the GSC is $\xi = 0.11$. The closed-loop poles of the system with the AD only implemented in the GSC are represented in blue in Fig. 15. It can be concluded that the damping of the resonant poles can be increased by implementing the AD in both converters at the same time, when a specific value of SCR is considered. This can be very helpful to comply with the current harmonic content limits enforced by certain grid codes. Table III shows a summary of the AD parameters that have been adjusted for each control strategy as well as the damping of the system resonant poles that is achieved in each case for a SCR of 20.

IV. Validation of the Proposed Active Damping Strategy

A. Experimental Results

In this subsection the interaction between the GSC and the RSC, the DFIG system model and the proposed AD strategy are validated. For this purpose, the experimental setup shown in Fig. 16 is built in the lab. The setup consists of a 5 kW doubly-fed induction generator, connected to a permanent magnet three-phase motor actuating as prime mover. This motor is controlled by a three-phase power converter that imposes the rotational speed of the mechanical shaft. Two 10 kW three-phase two-level power converters, namely the GSC and the RSC, are connected through the DC-bus to form a back-to-back structure. They are controlled by means of two Arduino Due and the DC-bus capacitors are connected to a DC source. The system parameters are the same as the ones used in the stability analysis, which appear in Table II. The switching and sampling frequencies are equal to 4 kHz. The tests are performed for two SCR values, 1 and 20.

First, the DFIG system is studied without any damping technique. The GSC current (purple) and the RSC current

TABLE III
Active Damping Parameters and Achieved Damping for a SCR of 20

Strategy	k_G	k_R	y_G	y_R	ξ
AD in GSC	16	0	0.617	0	0.11
AD in RSC	0	21	0	0.617	0.08
Combined AD	16	17	0.617	0.204	0.16

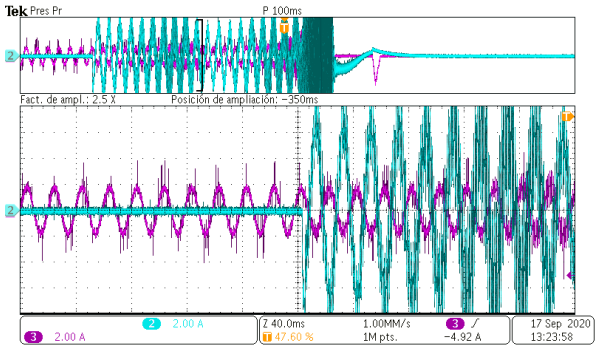

(a)

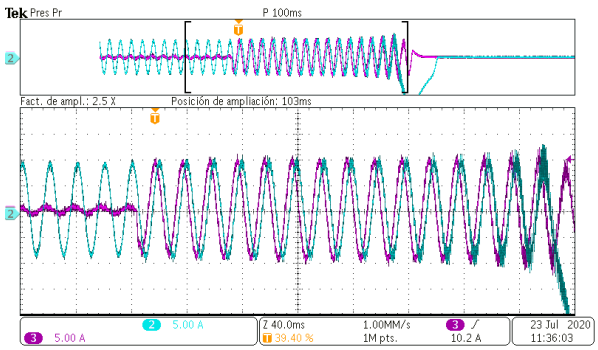

(b)

Fig. 17. GSC current (purple) and RSC current (light blue) without any damping strategy for a SCR of 1 (a) and 20 (b).

This article has been accepted for publication in a future issue of this journal, but has not been fully edited. Content may change prior to final publication. Citation information: DOI 10.1109/TPEL.2021.3089282, IEEE Transactions on Power Electronics

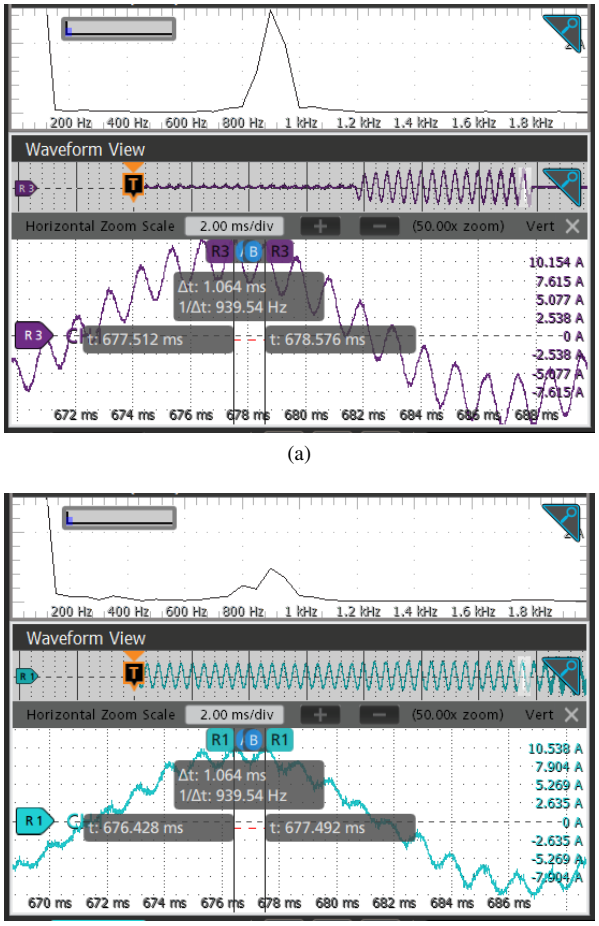

(a)

(b)

Fig. 18. Zoom to the last cycle of the GSC current (a) and the RSC current (b) before the converters disconnect for a SCR of 20.

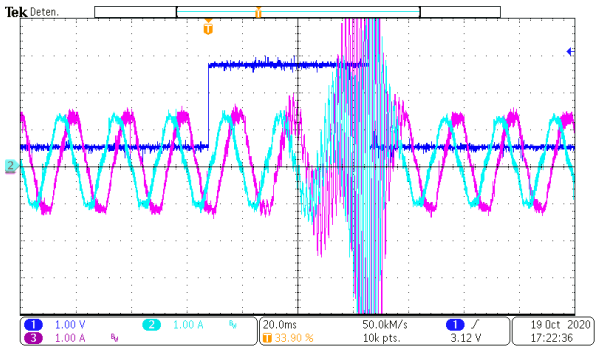

(a)

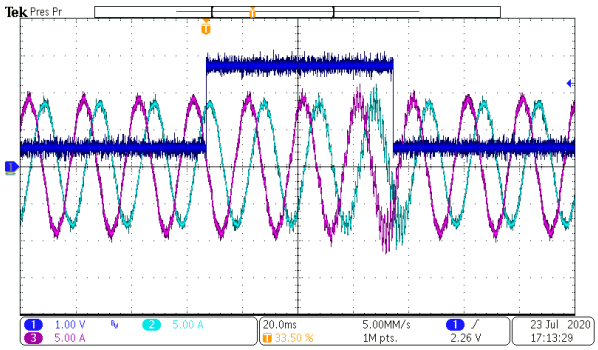

(b)

Fig. 19. GSC current (purple) and RSC current (light blue) when the AD strategy is activated and deactivated in the GSC for a SCR of 1 (a) and 20 (b).

(light blue) are shown in Fig. 17, for the two SCR values. For a SCR equal to 1, Fig. 17 (a), the GSC reference current is activated first and, after some time, the RSC is connected and its reference current is activated. As it is observed, the system is stable at the beginning when only the GSC is connected. However, when the RSC is activated the system becomes unstable. This interaction is also observed for a SCR of 20, as shown in Fig. 17 (b). Now, the reference current of the RSC is activated first and, then, the GSC is connected and its reference current is activated. It is observed that when the GSC is connected the system starts to resonate and, eventually, it becomes unstable. The last cycle of both converter currents before they disconnect is zoomed in order to determine the frequency of this resonance. As it is seen in Fig. 18 (a), where the GSC current is represented, the resonance frequency is 940 Hz. This is also verified by calculating the harmonic content of this waveform, which shows that there is a large harmonic around this frequency. The same analysis is done for the RSC current, which appears in Fig. 18 (b). The resonance frequency is also 940 Hz. In this case, the harmonic at this frequency is lower than in the GSC current, because it is more damped. This result validates the stability analysis performed in subsection II-C and confirms that there is an interaction between both converter control loops that must be considered to properly analyze the stability. Besides, for the SCR of 20, the instability appears close to 956 Hz, which is the DFIG system resonance frequency predicted by the model derived in subsection II-B for this SCR, and so, this model is validated.

Next, the proposed active damping strategy is validated. First, the AD is only implemented in the GSC with the parameters that have been adjusted in subsection III-B, $y_G = 0.617$ and $k_G = 16$. Fig. 19 shows the GSC current and the RSC current when the AD strategy is activated and deactivated in the GSC, which is indicated by the dark blue binary signal, for a SCR of 1 (a) and 20 (b). Initially, the AD is activated, stabilizing the system. At the rising edge of the dark blue signal, the AD is deactivated and the system starts to resonate at the system resonance frequency. After 4 cycles, the AD is reactivated (falling edge of the dark blue signal), stabilizing the system again.

The same test is performed to validate the AD strategy in the RSC with $y_R = 0.617$ and $k_G = 21$. Fig. 20 shows the GSC current, the RSC current and the signal that deactivates the AD for a SCR of 1 (a) and 20 (b). First, the AD is activated in the RSC. At the rising edge of the dark blue signal, the AD is deactivated and the system becomes unstable, resonating at the resonance frequency of the DFIG system. After some time the AD is reactivated, stabilizing the system. It is proved that the proposed active damping method effectively damps the system resonant poles when it is applied in either of the two converters, whether the DFIG wind turbine is connected to weak or strong grids. These results validate the theoretical analysis reflected in Fig. 12 and 14.

This article has been accepted for publication in a future issue of this journal, but has not been fully edited. Content may change prior to final publication. Citation information: DOI 10.1109/TPEL.2021.3089282, IEEE Transactions on Power Electronics

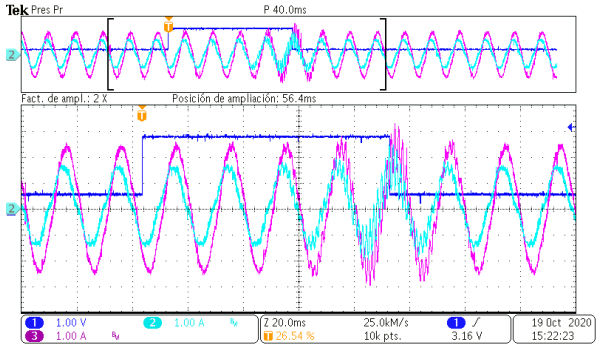

(a)

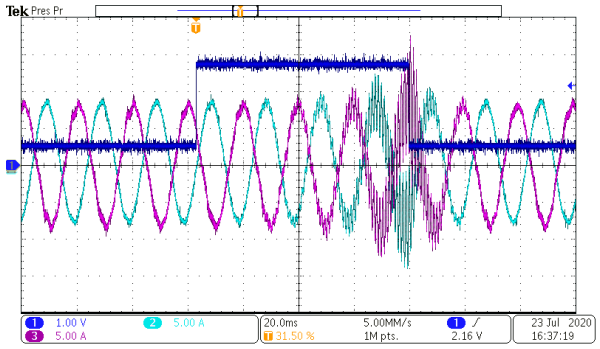

(b)

Fig. 20. GSC current (purple) and RSC current (light blue) when the AD strategy is activated and deactivated in the RSC for a SCR of 1 (a) and 20 (b).

Finally, the grid current harmonic content is analyzed with the AD implemented in the GSC and in both converters, as explained in subsection III-D. For that purpose, the harmonic currents are divided into integer harmonics and inter-harmonics, and compared to the limits given in the BDEW grid code [25]. Fig. 21 shows the comparison of the grid current harmonic content around the resonance frequency for a SCR of 20. As it is observed, when the active damping strategy is applied in both converters, the harmonic content is reduced since the system resonant poles are more damped in this case. These results validate the previous theoretical results from Fig. 15.

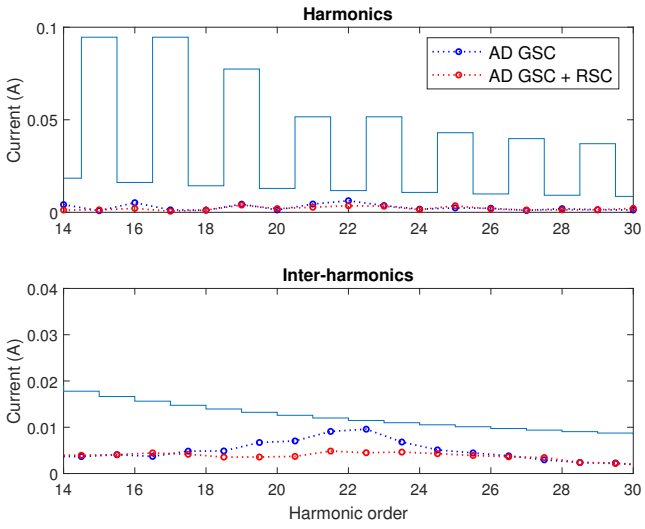

Fig. 21. Grid current harmonic content with the AD implemented in the GSC and in both converters for a SCR of 20.

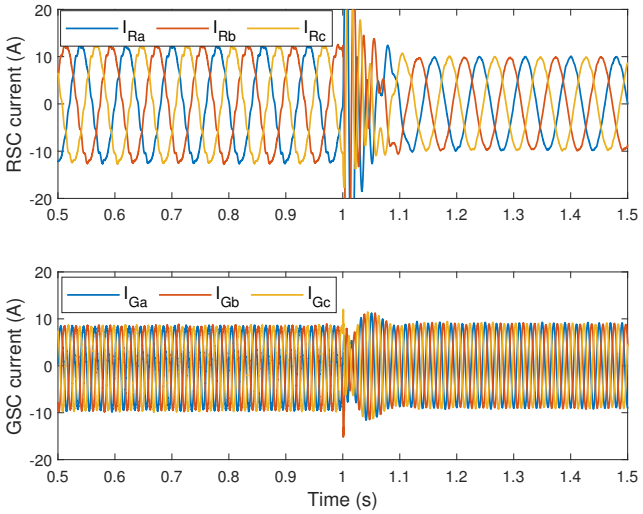

Fig. 22. RSC and GSC currents for a SCR of 20 when a voltage sag to 10 % occurs in the grid.

B. Large Signal Disturbance Validation

In this subsection the active damping strategy is tested under grid fault conditions. A voltage sag to 10 % of the nominal value is simulated at 1 s, with the AD strategy activated in both converters. The simulation is performed in Matlab/Simulink using the Simscape Electrical Library to create a model of the DFIG WECS. Fig. 22 shows the GSC and the RSC currents during the fault, proving that the DFIG system is stable.

The results in this section validate the proposed active damping method at different operating conditions.

V. Conclusion

In this work an active damping strategy based on the capacitor current feedback for a DFIG wind turbine with *LCL* filter is proposed. This paper is centered in two main aspects: the modeling of the DFIG wind turbine and the design of the AD strategy. A simplified plant model has been derived to analyze the interaction between the DFIG and the *LCL* filter impedances, which modifies the value of the resonance frequency. Besides, the GSC and the RSC control loops also interact with each other, which introduces a source of instability. Therefore, properly calculating the resonance frequency of the system and using a model that considers the interaction between the GSC, the RSC, the DFIG and the *LCL* filter, are key to design an effective AD strategy.

The proposed AD method stabilizes the system resonant poles and is robust against variations in the grid inductance, properly adjusting the delay of the feedback loop by means of a pure delay. It can be implemented in either of the two converters that form the back-to-back conversion structure connected to the DFIG's rotor windings. This increases the

flexibility of the control strategy since the AD can be activated in the converter that is more convenient, which may be the one that is further from saturation. Furthermore, the strategy can be applied in both converters simultaneously in order to maximize the damping for a specific grid inductance. For instance, several grid codes impose limits on the grid current harmonic content for a specific value of SCR at the PCC. In this case, it has been proved that by adjusting the delay of each converter we achieve a lower harmonic content in the grid current when the AD strategy is implemented in both converters at the same time.

ACKNOWLEDGMENT

This work was supported by the Spanish State Research Agency (AEI) under grant PID2019-110956RB-I00 /AEI/ 10.13039. The authors would like to thank Ingeteam Power Technology for its support.

REFERENCES

[1] V. Yaramasu, B. Wu, P. C. Sen, S. Kouro, and M. Narimani, "High-power wind energy conversion systems: State-of-the-art and emerging technologies," *Proceedings of the IEEE*, vol. 103, no. 5, pp. 740–788, 2015.

[2] H. Nian, P. Cheng, and Z. Zhu, "Coordinated direct power control of dfig system without phase-locked loop under unbalanced grid voltage conditions," *IEEE Transactions on Power Electronics*, vol. 31, no. 4, pp. 2905–2918, 2015.

[3] M. Liserre, F. Blaabjerg, and S. Hansen, "Design and control of an lcl-filter-based three-phase active rectifier," *IEEE Transactions on industry applications*, vol. 41, no. 5, pp. 1281–1291, 2005.

[4] R. N. Beres, X. Wang, M. Liserre, F. Blaabjerg, and C. L. Bak, "A review of passive power filters for three-phase grid-connected voltage-source converters," *IEEE Journal of Emerging and Selected Topics in Power Electronics*, vol. 4, no. 1, pp. 54–69, 2015.

[5] W. Wu, Y. Liu, Y. He, H. S.-H. Chung, M. Liserre, and F. Blaabjerg, "Damping methods for resonances caused by lcl-filter-based current-controlled grid-tied power inverters: An overview," *IEEE Transactions on Industrial Electronics*, vol. 64, no. 9, pp. 7402–7413, 2017.

[6] B. Liu, Q. Wei, C. Zou, and S. Duan, "Stability analysis of lcl-type grid-connected inverter under single-loop inverter-side current control with capacitor voltage feedforward," *IEEE Transactions on Industrial Informatics*, vol. 14, no. 2, pp. 691–702, 2017.

[7] J. Samanes and E. Gubia, "Active damping based on the capacitor voltage positive-feedback for grid-connected power converters with lcl filter," in *2019 21st European Conference on Power Electronics and Applications (EPE'19 ECCE Europe)*. IEEE, 2019, pp. P–1.

[8] J. Dannehl, M. Liserre, and F. W. Fuchs, "Filter-based active damping of voltage source converters with *lcl* filter," *IEEE Transactions on Industrial Electronics*, vol. 58, no. 8, pp. 3623–3633, 2010.

[9] E. Rodriguez-Diaz, F. D. Freijedo, J. C. Vasquez, and J. M. Guerrero, "Analysis and comparison of notch filter and capacitor voltage feedforward active damping techniques for lcl grid-connected converters," *IEEE Transactions on Power Electronics*, vol. 34, no. 4, pp. 3958–3972, 2018.

[10] W. Yao, Y. Yang, X. Zhang, F. Blaabjerg, and P. C. Loh, "Design and analysis of robust active damping for lcl filters using digital notch filters," *IEEE Transactions on Power Electronics*, vol. 32, no. 3, pp. 2360–2375, 2016.

[11] J. Samanes and E. Gubía, "Sensorless active damping strategy for parallel interleaved voltage source power converters with lcl filter," in *2017 IEEE Applied Power Electronics Conference and Exposition (APEC)*. IEEE, 2017, pp. 3632–3639.

[12] J. Roldán-Pérez, E. J. Bueno, R. Peña-Alzola, and A. Rodríguez-Cabero, "All-pass-filter-based active damping for vscs withlclfilters connected to weak grids," *IEEE Transactions on Power Electronics*, vol. 33, no. 11, pp. 9890–9901, 2018.

[13] W. Yao, Y. Yang, Y. Xu, F. Blaabjerg, S. Liu, and G. Wilson, "Phase reshaping via all-pass filters for robust lcl-filter active damping," *IEEE Transactions on Power Electronics*, vol. 35, no. 3, pp. 3114–3126, 2019.

[14] M. B. Saïd-Romdhane, M. W. Naouar, I. Slama-Belkhodja, and E. Monmasson, "Robust active damping methods for lcl filter-based grid-connected converters," *IEEE transactions on power electronics*, vol. 32, no. 9, pp. 6739–6750, 2016.

[15] D. Pan, X. Ruan, C. Bao, W. Li, and X. Wang, "Capacitor-current-feedback active damping with reduced computation delay for improving robustness of lcl-type grid-connected inverter," *IEEE Transactions on Power Electronics*, vol. 29, no. 7, pp. 3414–3427, 2013.

[16] Y. Lei, Z. Zhao, F. He, S. Lu, and L. Yin, "An improved virtual resistance damping method for grid-connected inverters with lcl filters," in *2011 IEEE Energy Conversion Congress and Exposition*. IEEE, 2011, pp. 3816–3822.

[17] X. Li, X. Wu, Y. Geng, X. Yuan, C. Xia, and X. Zhang, "Wide damping region for lcl-type grid-connected inverter with an improved capacitor-current-feedback method," *IEEE Transactions on Power Electronics*, vol. 30, no. 9, pp. 5247–5259, 2014.

[18] J. Liu, L. Zhou, and M. Molinas, "Damping region extension for digitally controlled lcl-type grid-connected inverter with capacitor-current feedback," *IET Power Electronics*, vol. 11, no. 12, pp. 1974–1982, 2018.

[19] S. He, J. Xiong, Z. Wang, and S. Lin, "Robust ad for lcl-type grid-connected inverter with capacitor current quasi-integral feedback," *IET Power Electronics*, vol. 13, no. 7, pp. 1332–1342, 2020.

[20] Y. He, X. Wang, X. Ruan, D. Pan, X. Xu, and F. Liu, "Capacitor-current proportional-integral positive feedback active damping for lcl-type grid-connected inverter to achieve high robustness against grid impedance variation," *IEEE Transactions on Power Electronics*, vol. 34, no. 12, pp. 12 423–12 436, 2019.

[21] Y. Song, X. Wang, and F. Blaabjerg, "High-frequency resonance damping of dfig-based wind power system under weak network," *IEEE Transactions on Power Electronics*, vol. 32, no. 3, pp. 1927–1940, 2016.

[22] H. Nian and B. Pang, "Stability and power quality enhancement strategy for dfig system connected to harmonic grid with parallel compensation," *IEEE Transactions on Energy Conversion*, vol. 34, no. 2, pp. 1010–1022, 2018.

[23] B. Pang, C. Wu, H. Nian, and F. Blaabjerg, "Damping method of high-frequency resonance for stator current controlled dfig system under parallel compensation grid," *IEEE Transactions on Power Electronics*, vol. 35, no. 10, pp. 10 260–10 270, 2020.

[24] Y. Song, X. Wang, and F. Blaabjerg, "Impedance-based high-frequency resonance analysis of dfig system in weak grids," *IEEE Transactions on Power Electronics*, vol. 32, no. 5, pp. 3536–3548, 2016.

[25] W. Bartels, F. Ehlers, K. Heidenreich, R. Huttner, H. Kuhn, T. Meyer, T. Kumm, J. Salzmann, H. Schafer, and K. Weck, "Generating plants connected to the medium-voltage network," *Technical Guideline of BDEW*, 2008.

[26] D. N. Zmood, D. G. Holmes, and G. Bode, "Frequency domain analysis of three phase linear current regulators," in *Conference Record of the 1999 IEEE Industry Applications Conference. Thirty-Forth IAS Annual Meeting (Cat. No. 99CH36370)*, vol. 2. IEEE, 1999, pp. 818–825.

[27] J. Samanes, A. Urtasun, E. L. Barrios, D. Lumbreras, J. López, E. Gubia, and P. Sanchis, "Control design and stability analysis of power converters: The mimo generalized bode criterion," *IEEE Journal of Emerging and Selected Topics in Power Electronics*, vol. 8, no. 2, pp. 1880–1893, 2019.

[28] Y. Song and F. Blaabjerg, "Overview of dfig-based wind power system resonances under weak networks," *IEEE Transactions on Power Electronics*, vol. 32, no. 6, pp. 4370–4394, 2016.